Noname manuscript No.
(will be inserted by the editor)

Magnetic properties of hematite with large coercivity

P. G. Bercoff[1] and H. R. Bertorello[1]

FaMAF, Universidad Nacional de Córdoba. IFEG, Conicet. Argentina.
E-mail: bercoff@famaf.unc.edu.ar

Received: date / Revised version: date

Abstract The magnetic properties of hematite powders produced by a solid state nucleation-and-growth process are studied as a function of temperature T and applied field H. Independently of the temperature, there exists a soft magnetic contribution that is assigned to the canting of spins at the superficial shell of each particle and is not affected by the Morin transition. At $220 < T < T_M$ a magnetic contribution with high coercivity is observed, due to spin–flop in the anti ferromagnetic state and above $T_M = 248$ K the weakly ferromagnetic state has a coercivity that ranges from 6 kOe to 4 kOe when raising T up to room temperature. Different sub-grain structures were obtained by means of isochronal and isothermal annealing. Changes in the susceptibility are directly related to the sub-particle size. It is concluded that sub-boundaries are the defects responsible for the high coercivities observed in the weakly ferromagnetic state.

PACS 75.47.Lx, 75.50.Tt, 91.25.F-, 91.60.Ed

1 Introduction

At low temperature, pure stoichiometric bulk hematite α-Fe_2O_3 is a collinear antiferromagnetic (AF) material, with spins aligned along the magnetically easy c-axis of its rhombohedral crystal structure. As the temperature increases, a magnetic transition is observed at $T_M \approx 265$ K. At this point the spins flop into the basal plane as a result of the antisymmetric Dzialoshinskii-Moriya exchange interaction, and take on a weakly ferromagnetic (WF) ordering with a spin canting of a fraction of a degree [1]. This phenomenon is called the *Morin transition* and occurs in both single-crystal and polycrystalline hematites. For these latter samples the Morin transition temperature T_M lowers with particle size and for sizes lesser than $\sim$ 20 nm the transition is fully suppressed. It has become commonplace to explain the occurrence of the Morin transition by a change of sign of the magnetocrystalline anisotropy when the temperature passes through T_M [2].

Large hematite single-crystals or particles in the 10μ–30μm size range have low coercivity due to their multidomain structure, in which the mechanism of domain wall displacement for magnetization reversal prevails [3]. According to Svoboda [4], depending on the microstructure of hematite particles, the coercivity H_c ranges between 0.3 kOe and 3 kOe. However, a few years earlier Dunlop [5] had already reported orange spheroidal natural hematite particles with coercivity as high as 5.2 kOe. Rath *et al.* [6] prepared pseudocubic, trapezoidal and hexagonal hematite particles of various sizes and studied the variation of the Morin transition temperature (T_M) and magnetic hysteresis parameters depending on the size and shape of the particles. Their pseudocubic-shaped particles of 650 nm showed an unusually high coercivity H_c of the order of 4 kOe, while for 60 nm hexagonal particles this value was reduced to 0.4 kOe. The origin of the observed high coercivities in hematite particles is still a matter of study and is certainly related to the internal microstructure. Rath *et al.* [6] found that their hematite particles were polycrystalline, formed by a large number of smaller crystallites (sub-particles) inside them. They found that the Stoner-Wohlfarth and non-magnetic grain boundary models are not applicable and they suggested that the origin of the observed high coercivity may be due to the large number of sub-particles inside their pseudocubic particles.

Nanocrystalline hematite produced by chemical routes [7] or by ball milling [8], has also been studied. If the crystals are very small, surface effects dominate the magnetic behaviour while if produced by ball milling a large concentration of defects is the responsible of much of the observed magnetic response. In the case of the chemical route, it is very difficult to assert that the final product is free from any of the characteristic radicals of the synthesis process which remain as defects in the structure. Mechanical alloying or mechanochemistry alone introduce severe damage in the lattice, leading to modified properties due to this complex structure deformation and degradation.

Here we want to report novel results on the magnetic properties of synthetic hematite particles with high crystallinity, obtained through a nucleation and growth process at high temperature. This route makes us anticipate the formation of pure hematite with high crystallinity. In previous works we noticed that the addition of pure Fe to a precursor powder of ferrite in a high-energy ball mill accelerates the extinction of the original crystals and promotes the formation of a precursor that, after heat-treating at high temperature, gives rise to small particles with a good crystalline phase [9,10]. We applied this idea to the present work. Our aim here is to shed some light on the origin of high coercivity in hematite particles with high crystallinity and its relationship with the internal microstructure.

2 Experimental

2.1 Sample preparation

Following the observation made in previous works [9, 10] regarding the preparation of small, highly crystalline particles, samples of hematite and pure iron mixed in different proportions were obtained by high-energy ball milling. Preliminary studies on all the prepared samples indicated that the sample with 20 wt.%Fe had the highest coercivity at room temperature, so this was the composition selected for this study. Sample F20 was obtained by milling 20 wt.% pure iron and 80 wt.% mineral hematite (micrometric sizes) in a Fritch Pulverizette 7 ball-mill for 4 hours, at 1400 rpm with a ball/powder ratio of 20. The as-milled powder was heat-treated for 1 hour at 1000°C in air atmosphere (sample F20p1) to obtain a fine black powder.

2.2 Sample characterization

X ray diffraction of the as-milled and the calcined powders were performed on a Philips diffractometer using CuKα radiation. The obtained spectra were refined using the program POWDER-CELL. Mössbauer spectroscopy at room temperature was performed on F20p1. A LEO 1450 VP scanning electron microscope (SEM) and an energy dispersive system (EDS) spectrometer Genesis 2000 were used to characterize the samples. SEM micrographs and EDS spectra were taken using an incident beam of 20 keV. Transmission electron microscopy (TEM) performed with a Philips CM-12 microscope operated at an accelerating voltage of 100 kV was used to observe the morphology and size of the particles.

Magnetic measurements were performed in a commercial SQUID Quantum Design (MPMS), with applied fields up to 30 kOe at different temperatures, from 7 K to 330 K. From the superior branch of each measured hysteresis loop the magnetic differential susceptibility χ was calculated as dM/dH.

Table 1 Mössbauer parameters: hyperfine field B_{hf}, isomer shift δ and quadrupole shift 2ϵ for sample F20p1 in this work, and for bulk [11] and milled [8] samples previously reported. ^{a}Measured at room temperature, affected by relaxation processes. ^{b}Measured at 17.7 K.

	F20p1	Bulk [11]	Milled [8]
B_{hf} [T]	52.41 ± 0.01	51.75 ± 0.01	40.8 ± 0.1^a
δ [mm/s]	0.33 ± 0.01	0.37 ± 0.01	0.48 ± 0.01^b
2ϵ [mm/s]	-0.20 ± 0.01	-0.197 ± 0.001	-0.19 ± 0.01^b

3 Results and discussion

3.1 Structure

The obtained XRD spectra are shown in figure 1. After the milling, the most intense diffraction peak of iron is still present, though with a very low intensity. The structure of hematite has disappeared as a result of the milling process and broad peaks corresponding to wüstite (FeO) reflections appear (see figure 1, bottom). After the heat-treatment, a very crystalline hematite is obtained (see figure 1, top). The refinement of the spectrum allowed us to determine that the sample is monophasic, with cell parameters $a = 5.034 \pm 0.002$ Å and $c = 13.743 \pm 0.002$ Å, and with a mean crystallite size of 140 nm. The observed cell parameters are coincident with those reported in the literature for bulk hematite [11] and very similar to the values reported by Mitra *et al.* [12] and Dang *et al.* [13] for pure hematite after 24 h at $T > 1000$°C. We explain this by considering that in our case the milling process produces a great number of nucleation centers, originating small particles during the annealing process at $T = 1000$°C. One hour of annealing was enough for obtaining small, highly crystalline particles.

The Mössbauer diagram obtained at room temperature is shown in figure 2. A very "clean" spectrum is obtained, consisting of a sextet that indicates the presence of Fe^{3+}. Table 1 gives the parameters of the fitting for the sextet (hyperfine field B_{hf}, isomer shift δ and quadrupole shift 2ϵ), as well as the ones for bulk hematite at room temperature [11] and for milled hematite [8] at room temperature (B_{hf}) and 17.7 K (the rest).

The Mössbauer parameters for sample F20p1 are in agreement with the ones for bulk hematite, and differ from the ones for the structure with defects produced by milling and no posterior thermal treatment (see Table 1), indicating high crystallinity. No relaxation processes as a consequence of structural damage nor particle-size effects are noticed in the spectrum of figure 2. The quadrupole shift of −0.20 mm/s indicates that the system is in the weakly ferromagnetic phase

[14]. According to EPMA results, the samples contain pure hematite with no cation substitutions in the structure. Therefore, the slight increase in hyperfine field B_{hf} is attributed to the presence of structural defects alone.

Figure 3a shows TEM micrographs where an ellipsoidal particle 300-400 nm in size (left) and an ellipsoidal together with a rhombohedral particle (right) are shown. Figures. 3b and c are SEM images at different magnifications. It is possible to observe different degrees of agglomeration among the particles, resulting in conglomerates of sizes ranging 5 μm to 200 μm. It is interesting to note that there are two different particle shapes — the ellipsoidal and the rhombohedral, with faceted faces and sharp edges. Figure 3d is an EPMA spectrum taken from the sample, which shows that there are no noticeable impurities.

Figure 4 shows a histogram of the particle sizes, measured from SEM micrographs as the one shown in figure 3c. The mean size is around 1 μm, which is a much larger value than the mean crystallite size of 140 nm obtained from XRD. From this data we infer that the ellipsoidal/rhombohedral particles are in fact polycrystalline with a substructure –these particles contain smaller crystallites (sub-particles) inside them. The mentioned values allow us to estimate a number of 45 sub-particles within each particle of hematite. Similar polycrystalline behaviour was reported earlier for pseudocubic particles of hematite by other authors [6], who find coercivities of the order of 6 kOe when there are a great number of smaller sub-particles (over 150,000 of around 20 nm) within one micron-sized particle.

3.2 LTC

Low temperature cycling (LTC) consists of a zero-field cooling and warming of the sample while measuring the magnetization. This curve was measured after applying a field of 3 T at room temperature, on cooling from room temperature down to 5 K and then back to room temperature (figure 5). From the heating curve, the Morin transition temperature (T_M) was obtained as the maximum of the derivative dM/dT (see inset of figure 5) yielding $T_M = 248$ K. A $\Delta T_M = 8$ K at T_M is measured between the cooling and the heating curves. It is also noticed that the Morin transition does not occur sharply but comprises a wide range of temperatures starting at $T_i = 200$ K and ending at $T_f = 275$ K, as shown in figure 5 and its inset. The resulting Morin temperature for the studied samples T_M=248 K is lower than the value for the bulk (265 K [1,11]). The observed hysteresis between the cooling and heating curves ΔT_M=8 K agrees with this value for powders since single crystals display $\Delta T_M \sim$ 1-5 K [1]. It is mentioned in the literature that $\Delta T_M \sim 0$ K corresponds to single crystals without defects [1]. It is possible that a higher value of ΔT_M in powders might be associated to the spin canting on the surface of the particles.

Variations in both T_M and the extent of the transition $T_f - T_i$ have been observed as a result of the presence of OH groups, sulphures and substitutional cations (see, for instance, Ref. [13]). It was observed that T_M increases and $T_f - T_i$ decreases as both annealing temperature and annealing time increase, due to a faster annihilation of defects at higher temperatures. It has also been reported by different authors [1,11,15,16] that T_M decreases as the particles size is reduced, and the Morin transition disappears for sizes below 20 nm. This is associated to surface effects that lead to spin canting at the particles surface, low crystallinity, vacancies and stoichiometric deviations [13]. In our case, the extent of the transition $T_f - T_i$ is quite large (see figure 5 and its inset) and this is directly related to the wide particles size distribution (figure 4).

Below T_i a rather high value of magnetization is measured, considering that the system is in the AF state and the expected value for M in this state is zero. In this case, it is $M_{\mathrm{AF}} = 13\% M_{\mathrm{WF}}$. Özdemir and Dunlop [17] find that M_{AF} is 1–3 % of M_{WF} for synthetic submicron hematites and they attribute this to a "defect ferromagnetism" which arises from the microstructural defects and/or impurities and which is not affected by the Morin transition. They state that the moment originated in the defects is the responsible for the memory effect observed at temperatures above T_M in LTC and LTD (low temperature demagnetizing) experiments. The memory effect is directly linked to the magnetization of the defects which are not altered by changes in T through T_M, and act as nucleation centers for magnetization in the WF state. In our samples, the higher recovery after LTC (73% compared to 40%) is related to the higher M_{AF}, since there would be more nucleation centers to drive the magnetization back to its state before LTC. A more detailed study of this effect on similar hematite samples has been already published [18].

3.3 Mvs.H

For all T, magnetization is described by considering three contributions: 1. a paramagnetic background, 2. a soft ferromagnetic part and 3. a hard ferromagnetic component.

Figure 6 shows the curves M vs. H measured at temperatures between 7 K and 200 K. They are all similar and exhibit a main paramagnetic behaviour with a small ferromagnetic component. There is a slight change in the slope of the curve at 20 kOe, indicating a "spin flop" process is occurring at this field [19–21]. In our case, the spin flop field H_{sf} is not strongly temperature-dependent since its value is around 20 kOe for temperatures ranging from 7 K to 200 K. The same value of H_{sf} has also been reported by other authors [12].

The magnetic differential susceptibility χ is defined as the derivative dM/dH, and its spectrum is associated to the inversion-field distribution in the sample.

The inset in figure 6 shows the susceptibility at $T = 7$ K. There is a sharp maximum at the origin corresponding to a small fraction of the sample with soft ferromagnetic behaviour. The slope of χ increases for high fields. The same behaviour is observed for all temperatures from 7 K to 200 K.

Figure 7a displays the curves M vs. H for $T = 220$, 230 and 240 K and figure 8a for $T = 270$, 290 and 330 K. The corresponding susceptibilities are shown in figure 7b and figure 8b, respectively.

The following observations can be pointed out:

1. The paramagnetic background has a susceptibility $\chi = 16 \times 10^{-6}$ emu/gOe at low fields and $T < 230$ K, and $\chi = 20 \times 10^{-6}$ emu/gOe for $T > T_M$. In hematite single crystals the magnetic susceptibility χ takes different values depending if the applied field H is applied parallel or normal to the $< 111 >$ axis, being $\chi_{\|}^{\mathrm{AF}} = 2 \times 10^{-6}$ emu/gOe and $\chi_{\perp}^{\mathrm{AF}} = 18 \times 10^{-6}$ emu/gOe for $T < T_M$ [1]. Our value of $\chi = 16 \times 10^{-6}$ emu/gOe is lower than $\chi_{\perp}^{\mathrm{AF}}$ and higher than $\chi_{\|}^{\mathrm{AF}}$ because the particles are randomly oriented. For $T > T_M$ both $\chi_{\|}^{\mathrm{WF}}$ and $\chi_{\perp}^{\mathrm{WF}}$ are very similar, being $\chi_{\|}^{\mathrm{WF}} = 20 \times 10^{-6}$ emu/gOe and $\chi_{\perp}^{\mathrm{WF}} = 18 \times 10^{-6}$ emu/gOe. Our values of susceptibility for temperatures above T_M $\chi(T > T_M) = 20 \times 10^{-6}$ emu/gOe agree with the reported results for the WF phase of hematite and remain constant with the applied field. However, for temperatures below 200K a change in the slope of the M vs. H curves is noticeable at a field of 20 kOe (figure 6), similarly to the results obtained by Fiorani *et al.* [20] and Zysler *et al.* [21]. This change in the M vs. H slope is interpreted as the first signals of spin flop in the antiferromagnetic phase.
2. The soft ferromagnetic contribution is noticed as a peak in χ centered in ${}_{\chi}H_c \approx 130$ Oe, which is almost constant along the whole T range and whose area does not exceed the 10% of the total area under the χ vs. T curve. Since this contribution is not altered when going through T_M, it is not possible to identify it either with the AF state contribution for $T < T_M$ nor with the WF state contribution for $T > T_M$. Because of its "soft" nature and small share in the total magnetization we state that this contribution originates in the superficial shell of each particle which is affected by spin canting, having lower anisotropy and a different magnetic state than that of the core. Because this contribution is unaltered by changes in T we infer it is only weakly coupled to the spins within the core.
3. As the temperature increases from 220 to 240 K, the magnetic behaviour changes in nature and the sample starts showing considerable hysteresis (figure 7a). The susceptibility reflects this transition and moves from the typical profile observed at low temperatures to a different one, with two maxima —one around 130 Oe (which corresponds to the soft contribution) and another much harder peak (the hard contribution) which gradually softens from 30 kOe at 220 K to 5 kOe at 330 K (see figure 8b). The position of the "hard" and "soft" peaks (${}_{\chi}H_c^{\mathrm{hard}}$ and ${}_{\chi}H_c^{\mathrm{soft}}$, respectively) as a function of T is shown in figure 9.
   The hard ferromagnetic contribution has a wide distribution of inversion fields which range from 4 to 6 kOe for $T > T_M$ and from 8 to 30 kOe for 220K$< T < T_M$ (see figure 9) and comprises around 90% of the total area under the χ vs. T curve.
   In the range $T_i - T_f$ there coexist particles in the AF and in the WF states, so the magnetic response is the sum of both states contributions.
   For $T_i < T < T_M$ the appearance of an important peak in the susceptibility χ is observed, whose maximum moves to lower fields with increasing T. This behaviour, depicted in figure 9, is similar to the behaviour of $H_{c\perp}$ and $H_{c\|}$ in hematite single crystals in the same temperature range [1] and therefore we assign the "hard" peak in χ, ${}_{\chi}H_c^{\mathrm{hard}}$, to spin flop of the AF phase. The inversion field distribution (closely related to the profile of χ vs. H) modifies its profile and shifts to lower fields with increasing T, up to T_M. From this temperature on, the inversion field distribution keeps its profile constant and the displacement of the maximum is less pronounced. We interpret this considering that the system in the WF state has a high coercivity because of the presence of defects which act as pinning centers and hinder the magnetization reversal by coherent rotation within the core of each particle. Since the mean particle size is 1 μm, we disregard domain wall displacement as a possible magnetization reversal mechanism because the critical single-domain size of hematite is in the range 10 - 100 μm [5].

3.4 Thermal treatments

As it was stated in Section 3.3, the soft and T-independent component of the χ spectrum is assigned to the defects moment of the superficial shell in each particle. The inversion field distribution observed at high H above T_M is assigned to the WF state in each particle and must be related to the presence of defects in the particles' core.

In order to give another suport to this statement, different thermal treatments were performed on F20. Let us recall that sample F20p1 had been obtained by heating the precursor F20 for 1 hour at $T = 1000°$C. The precursor F20 was also heat-treated for 1 hour at 1100°C (sample F20q1) and 1200°C (sample F20r1), and for 3 hours at $T = 1000°$C (sample F20p3) in order to compare isochronal as well as isothermal treatments. The susceptibilities of the resulting samples are shown in figure 10a for the isochronal case and in figure 10b for the isothermal case. Depending on the kind of treatment (isochronal or isothermal) there is a marked difference in the resulting susceptibility. When the heating temperature is raised to 1100°C and 1200°C, ${}_{\chi}H_c^{\rm hard}$ is shifted to lower fields and the softer peak around the origin, ${}_{\chi}H_c^{\rm soft}$, remains exactly the same, both in position and amplitude. On the other hand, when the heating time is tripled but the temperature is held constant in 1000°C, ${}_{\chi}H_c^{\rm hard}$ is displaced towards higher fields, reducing its values at lower fields and increasing the ones at higher fields. The small peak around the origin ${}_{\chi}H_c^{\rm soft}$ remains unchanged, just as in the isochronal case.

Figure 10c shows the variation of sub-particle size as revealed by x-ray diffraction. During isothermal annealing at $T = 1000$°C the sub-particle size remains almost unchanged from 1 to 3 h, while isochronal annealing at 1000°C, 1100°C and 1200°C produces an enlargement of the sub-particles from 140 nm at 1000°C to 300 nm at 1200°C.

Both in the isochronal and isothermal cases, the changes in the harder peak would be related to the efficiency of the defects as pinning centers against the coherent rotation of the WF moments in the core, since thermal treatments allow the diffusion of defects through the lattice, softening the sample. The results of the diffusion process are however different, since raising the temperature softens the harder peak leaving the soft one unchanged (figure 10b), while increasing the treatment time at the same temperature also leaves the soft peak unchanged but the harder peak is displaced towards higher fields (figure 10a). These results must be related to the changes in sub-particle size produced by the annealing process and shown in figure 10c.

The changes in the profile of inversion fields are certainly related to the nature of the defects in the structure and to their evolution according to the different annealing processes. The different inversion field spectra have a wide peak at high H, with important contributions at low fields. This indicates a continuous distribution of energy barriers for magnetization reversal, which could be originated in:

i. *Shape anisotropy*: it is proportional to M_s and can be neglected in hematite [3].

ii. *Magnetocrystalline anisotropy*: it originates coercivities from 10 Oe for large, multidomain grains to several kOe in single domain particles. It depends weakly on T in the WF state and cannot explain the large variations observed in χ.

iii. *Magnetostrictive anisotropy*: the most probable source is internal stresses. Magnetostriction in hematite is $\lambda_s \approx 8 \times 10^{-6}$ and taking $H_c = \frac{3}{2}\lambda_s\, P\, M_s$, with $P = 100$ MPa being the internal stress expected in the vicinity of dislocations, a value of ~ 5000 Oe is obtained [3, 5].

This observation leads us to analyze the different kind of defects which could be associated with the annealing experiments results. Each kind of defect is related to a corresponding magnetization, originated in the canting of the localized moments of each magnetic sublattice which is affected by the deformation field produced by the defect. The canting of the defect moments produces an extra magnetization when compared to the magnetization of the WF phase without defects. The deformation field and the magnetoelastic effect produced by a defect will modify the free energy of the defect, which will have a minimum for a certain equilibrium orientation distribution of the moments associated with the defect. If we want to invert the magnetization associated to a certain defect, we would have to overcome an energy barrier which is related to magnetoelastic anisotropy, which is characteristic of each kind of defect and which will increase the coercivity H_c above the value it would have for a defect-free structure. In general, a certain sample will have a kind-of-defects distribution each having a particular elastic field. We can anticipate that concentrated and coherent defects (such as point defects) will have lower magnetoelastic anisotropy since the energy of the defect depends on the volume it affects, and its influence on H_c will be weak. Incoherent defects do not have an elastic field associated and therefore no magnetoelastic anisotropy, so these kind of defects will have no effect on the coercivity. On the other hand, coherent extended defects (such as low-angle grain boundaries, dislocations pile-ups and sub-grain boundaries) are likely to produce a considerable raise in H_c because their free energy is high due to the extension of the deformation field and high magnetoelastic anisotropy.

According to the discussion of Section 3.1, we may consider that the particles with a mean size of 1 μm have a structure of sub-particles or sub-grains of 140 nm. These sub-particles are probably separated by low-angle grain boundaries, some of them consisting of border dislocations pile-ups while others being of mixed nature: border and screw dislocations. These arrangements will have different mobilities and hence will be affected differently by thermal fluctuations. Also, the particles will have point and volumetric defects distributions.

We may explain the behaviour observed in figure 10 by considering the defects as pinning centers for coherent rotation of the magnetic moments in each particle. The results shown in figure 10a can be understood by considering that annealing for 1 h at 1000°C produces a metastable structure. When the annealing time is extended to 3 h, point defects are able to migrate towards the particle surface and grain boundaries, resulting in a lower χ at low H. At the same time, grain sub-boundaries evolve towards a more stable configuration and practically not changing the sub-particle size d (see figure 10c). These more stable sub-boundaries have lower free energy and a higher energy barrier must be overcome for magnetization reversal, leading to a rise in χ at high H.

On the other hand, the curves shown in figure 10b are the result of the evolution towards a state with less sub-particles, as implied by the increase in d shown in figure 10c. With less sub-boundaries in each particle, the pinning centers hindering magnetization reversal will be less, leading to lower χ at high H. This is because the sub-boundary area A_{sb} in each particle is a function of the number of sub-particles per particle $N_{sp} \sim V_p/d^3$ (being V_p the particle volume) and $A_{sb} \sim N_{sp}d^{2/3} = V_p d^{-7/3}$, therefore $A_{sb} \sim d^{-7/3}$. Then, χ diminishes at high H. At the same time, the dissolution of sub-grain boundaries produces a larger number of point defects migrating towards the particle surface, and this results in higher χ at low H.

The small peak in χ located at the origin remains constant regardless of the thermal treatment. This is consistent with the assumption made that ${}_{\chi}H_c^{\mathrm{soft}}$ is caused by the moment of the particle's shell.

4 Conclusions

By means of a nucleation and growth process in the solid state, we were successful in obtaining single-domain hematite particles with a sub-particle structure, high crystallinity and structural parameters that correspond to bulk hematite. The obtained particles present the following characteristics:

1. A paramagnetic behaviour for the AF state at $T < T_M$ and for the WF state at $T > T_M$.
2. In the AF state, the first signs of spin flop are noticed at $H \sim 20$kOe.
3. A soft ferromagnetic contribution is found at all T and is assigned to the magnetic moments lying in the superficial shell of each particle.
4. There are two hard ferromagnetic contributions:
   (a) At $220K < T < T_M$, a wide distribution of inversion fields ranging from 8 to 30 kOe is observed, whose dependance on T is similar to the behaviour of $\chi_{\parallel}$ and $\chi_{\perp}$ in single crystals of hematite. This is assigned to spin flop in the AF state.
   (b) At $T > T_M$, a distribution of inversion fields ranging from 4 to 6 kOe is observed in the WF state. The origin of this coercivity is assigned to the role of defects.
5. Hematite with high coercivity has a high memory effect ($\sim 70\%$) after saturation and isothermal remanent magnetization, in contrast to $\sim 40\%$ recovery observed by other authors.
6. Isochronal and isothermal annealing experiments lead us to conclude that the origin of the observed high coercivities is the presence of a sub-particle structure and the associated stress fields at the sub-particles boundaries.

The results obtained in this work with synthetic hematite particles may be applied to the study of natural hematite. We can infer that natural hematites with high coercivity were originated at low temperatures, while crystals with low coercivities were at temperatures around and above 1000 °C for long enough time to eliminate structural defects.

Acknowledgements

The authors acknowledge SECYT - UNC, CONICET AND FONCYT for the financial support and to the "Red Nacional de Magnetismo y Materiales Magnéticos" (RN3M) for providing the equipment to perform the magnetic measurements.

References

1. A. Morrish: Canted Antiferromagnetism: Hematite (World Scientific Publishing Company, Singapore 1994)
2. P. Besser, A. Morrish, C. Searle: Phys. Rev. **153** 632 (1967)
3. D. J. Dunlop, Ö. Özdemir: Rock Magnetism. Fundamentals and Frontiers (Cambridge University Press 1997) p 72
4. J. Svoboda: Magnetic Methods for the Treatment of Minerals: Development in Mineral Processing vol 8 (Elsevier Science, Amsterdam 1987) p 44
5. D. J. Dunlop: Ann. Geophys. No 3 **27** 269 (1971)
6. C. Rath, K. K. Sahu, S. D. Kulkarni, S. Anand, S. K. Date, R. P. Das, N. C. Mishra Appl. Phys. Lett. No 26 **75** 4171 (1999)
7. R. Zysler, M. Vasquez-Mansilla, C. Arciprete, M. Dimitrijewits, D. Rodríguez-Sierra, C. Saragovi: J. Magn. Magn. Mat. **224** 39 (2001)
8. R. Borzi, S. Stewart, G. Punte, G. Mercader, M. Vasquez-Mansilla, R. Zysler, E. Cabanillas: J. Magn. Magn. Mat. **39** 205 (1999)
9. P. G. Bercoff, H. R. Bertorello: J. Magn. Magn. Mat. **187** 169 (1998)
10. P. G. Bercoff, H. R. Bertorello: J. Magn. Magn. Mat. **205** 261 (1999)
11. R. Cornell, U. Schwertmann: The iron oxides (VCH Weinheim 1996)
12. S. Mitra, S. Das, S. Basu, P. Sahu, K. Mandal: J. Magn. Magn. Mat. **321** 2925. DOI: 10.1016/j.jmmm 2009.04.044 (2009)
13. M. Z. Dang, D. G. Rancourt, J. E. Dutrizac, G. Lamarche, R. Provencher: Hyperf. Inter. **117** 271 (1998)
14. E. Van San, E. De Grave,R. E. Vandenberghe: J. Magn. Magn. Mat. **269** 54 (2004)
15. N. Amin, S. Arajs: Phys. Rev. B **35** 4810 (1987)
16. Ö. Özdemir: American Geophysical Union, Fall Meeting 2007 abs.No.GP24A-02 (2007)
17. Ö. Özdemir, D. J. Dunlop: Geophys. Res. Lett. No 18 **29** 1877 (2002)
18. P. G. Bercoff, H. R. Bertorello, M. I. Oliva: Phys. B: Physics of Cond. Matt. **398** 204 (2007)
19. P. Besser, A. Morrish: Phys. Lett. **13** 289 (1964)
20. D. Fiorani, A. M. Testa, L. Suber, M. Angiolini, A. Montone, M Polichetti: Nanostr. Mater. **12** 939 (1999)
21. R. Zysler, D. Fiorani, A. M. Testa, L. Suber, E. Agostinelli, M. Godinho: Phys. Rev. B **68** 212408 (2003)

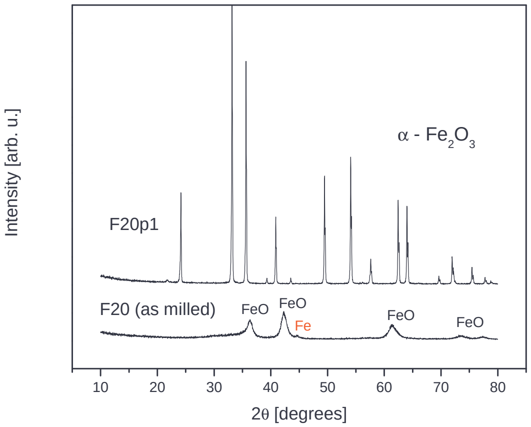

Fig. 1 X-ray diffraction patterns of sample F20 (bottom) and sample F20p1 (top). All the peaks observed in this diffractogram correspond to α-Fe_2O_3, with no reflections from other phases.

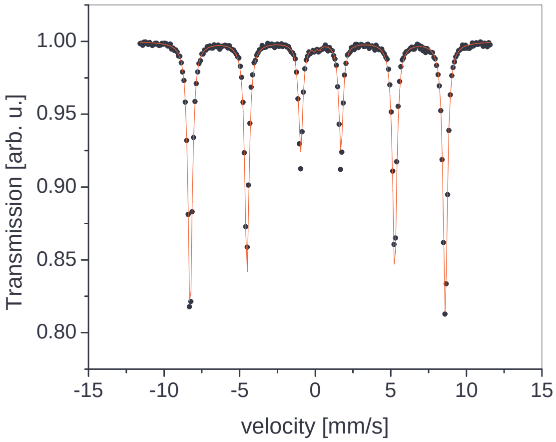

Fig. 2 Room temperature Mössbauer spectrum of sample F20p1.

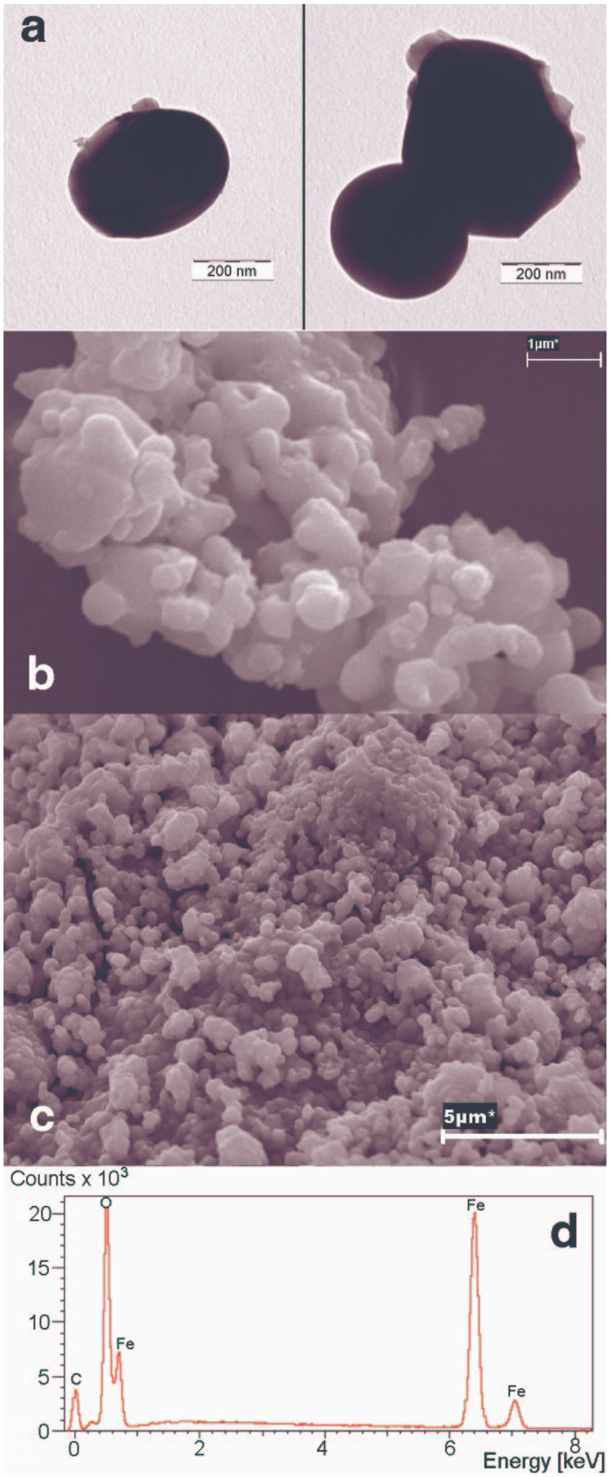

Fig. 3 Microstructure of F20p1. a) TEM micrographs illustrating the characteristic particle morphologies. b) and c) SEM images at different magnifications. d) EPMA spectrum.

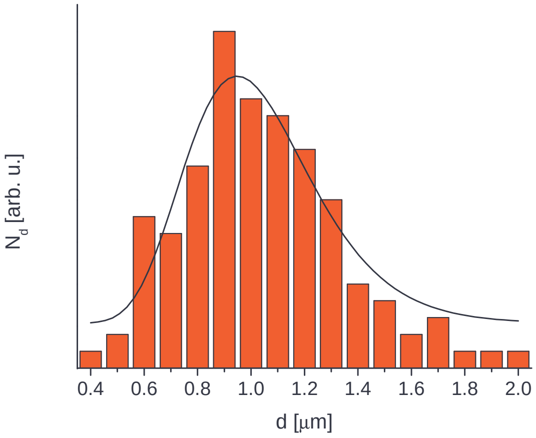

Fig. 4 Particle size distribution based on data taken from SEM measurements. The solid line corresponds to a log-normal function, with mean $< d >= 1.0$ and $\sigma = 0.2$.

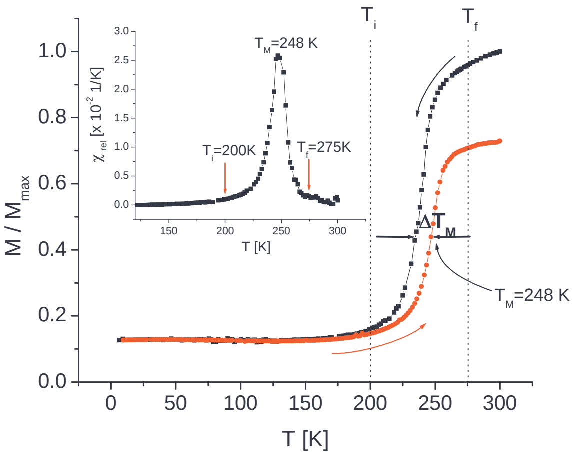

Fig. 5 LTC curve measured for F20p1 with no applied field. The inset shows the derivative dM/dT, whose maximum is at the Morin temperature T_M. Temperatures $T_i = 200$ K and $T_f = 275$ K, the initial and final temperatures of the transition, respectively, are shown with dotted lines and arrows in the inset.

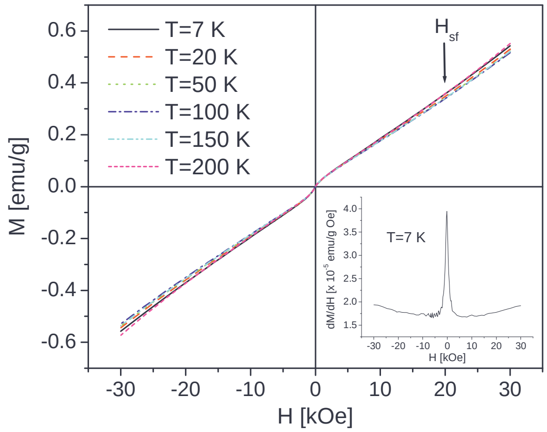

Fig. 6 M vs. H measured at temperatures between 7 K and 200 K. The inset shows the susceptibility at $T = 7$ K.

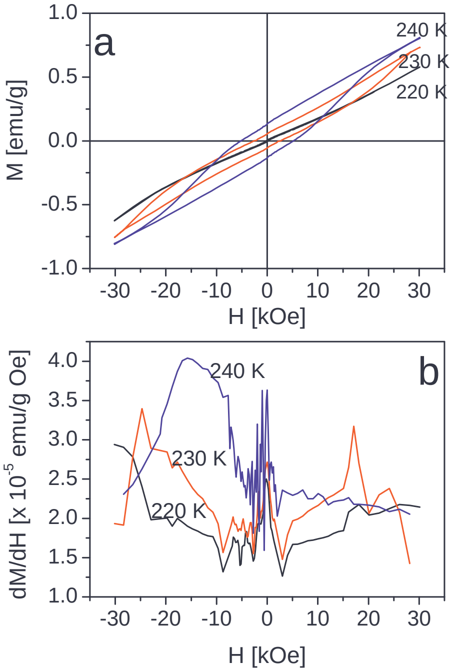

Fig. 7 M vs. H (a) and χ (b) for $T = 220$, 230 and 240 K

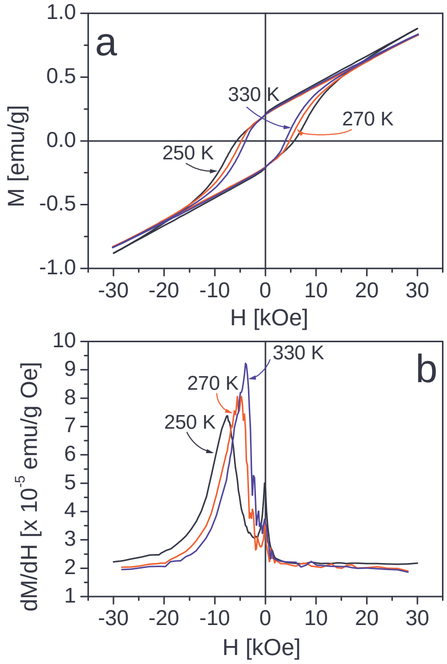

Fig. 8 M vs. H (a) and χ (b) for $T = 250$, 270 and 330 K

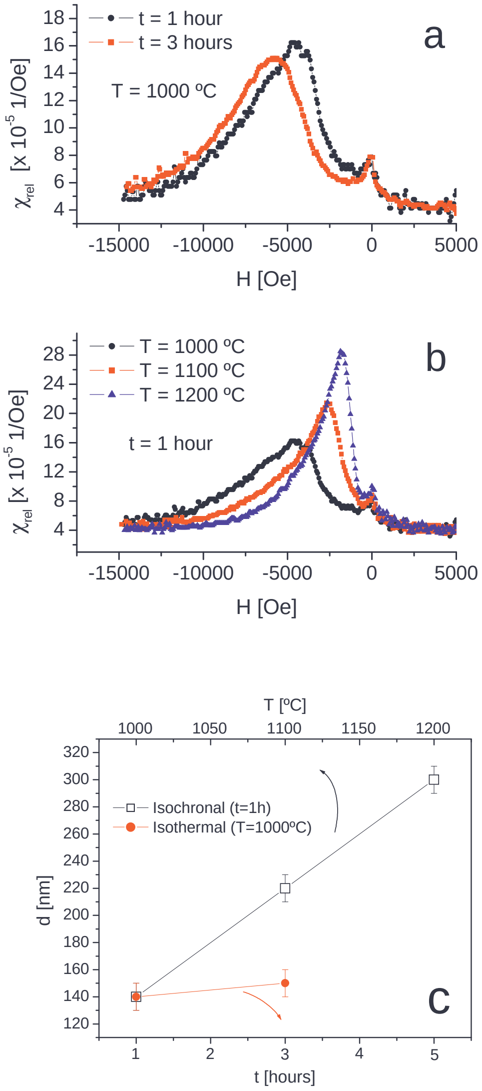

Fig. 10 Susceptibility of the samples after isothermal (a) and isochronal (b) annealing. c) Sub-particle size as revealed by x-ray diffraction for isochronal (upper axis) and isothermal (bottom axis) annealing.

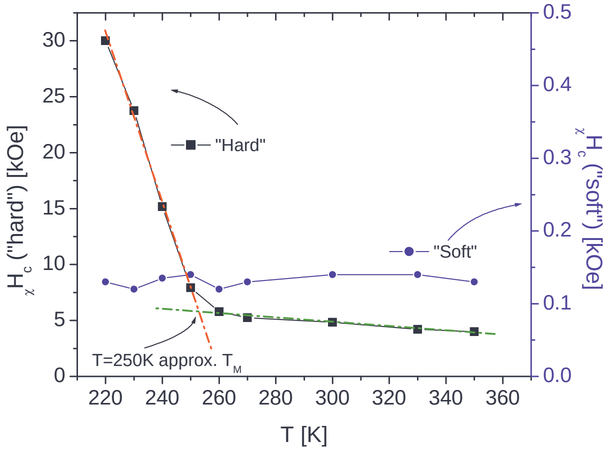

Fig. 9 Position of the "hard" ($_{\chi}H_c^{\mathrm{hard}}$) and "soft" ($_{\chi}H_c^{\mathrm{soft}}$) peaks as a function of T, in the left and right axis, respectively.